Defects analysis in LPBF printing based on up-skin and down-skin angles using machine learning

Zohreh Azimifar[1], Ali Razani[2], Sagar Patel[1], Martine McGregor[1], and Mihaela Vlasea[1,*]

[1] Department of Mechanical and Mechatronics Engineering, University of Waterloo, Waterloo, Canada

[2] Department of Computer Science and Engineering, Shiraz University, Shiraz, Iran

* mihaela.vlasea@uwaterloo.ca

Abstract: In laser powder bed fusion (LPBF) additive manufacturing, geometric features of parts have a significant impact on their printability and quality. Special attention in the literature has been given to the characteristic feature of distinction between up-skin and down-skin surface properties, where up-skin and down-skin surfaces have different orientation angles with respect to the build plate during part fabrication. We focus on slice-level, surface-connected defect analysis relative to up- and down-skin orientation using a YOLO→U-Net pipeline, followed by clustering and statistical morphology. We use a dataset acquired by X-ray CT scanning of LPBF-manufactured Ti–6Al–4V (Ti64) parts and 3D lattice structures with segmented regions of the top and bottom skins. This design allows slice-level analysis of defect geometry with respect to surface-normal direction. Lattice architectures with strut-based and surface-based features with a cell size of 2 mm and strut/wall thickness between 0.25-0.55 mm were utilized in this study. Machine learning and deep learning techniques such as YOLO and U-Net have significantly contributed to the precision and effectiveness of defect and pore detection and classification in 3D-printed components. Outcomes are expected to enhance the defect formation mechanism knowledge and allow optimization of print and design parameters toward improved quality and reliability of key application 3D printed parts.

Keywords: Additive Manufacturing, Machine Learning, Down-skin, Up-skin, LPBF

1. Introduction

Laser Powder Bed Fusion (LPBF) is a leading metal additive manufacturing process that builds parts layer by layer by selectively melting metal powder with a focused laser beam [1,2]. In LPBF, the relative position of every surface to the build plate results in down-skin and up-skin regions: down-skin surfaces, i.e., those features with surface angle 0° to 90° with respect to the build plate (especially below 45°), are prone to poor fusion, increased porosity, and roughness of the surface caused by lack of support; however, up-skin surfaces, having angles 90° to 180°, are self-supporting and are likely to possess improved geometric fidelity and surface finish [3,4]. This clear distinction highlights the critical need of design optimisation and process-parameter control—and invites machine-learning and deep-learning designs—to accurately predict and prevent skin-specific defects in complex LPBF-fabricated geometries [5-7]. X-ray CT scans of Ti–6Al–4V lattice structures show that down-skin areas often are full of irregular, finger-like defects and clusters of dross along unsupported overhangs, whereas up-skin regions are largely covered with small, rounded defects by gas entrapment in well-supported melt pools. These surface orientation-dependent defect morphologies influence mechanical performance and fatigue life and underscore the necessity for advanced machine-learning methods for quantifying, classifying, and eventually predicting defect formation as a function of surface orientation [8,9].

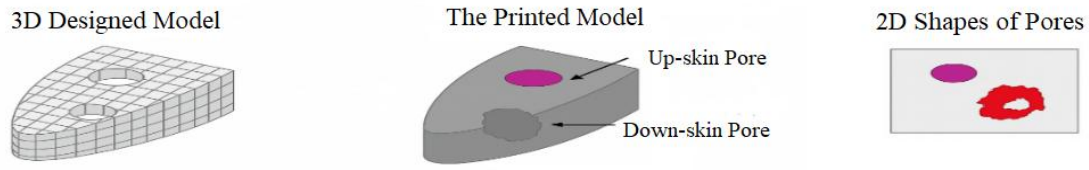

Figure 1. After printing, pores in down-skin regions are larger and asymmetric due to insufficient support and instability in the melt pool, whereas pores in up-skin regions are smaller and more symmetric.

2. Materials and methods

This section outlines data preparation and the detection–segmentation workflow for CT-based defect analysis.

2.1. Data preparation

The data preparation pipeline involves specimen fabrication, micro-CT imaging, and preprocessing of CT slices.

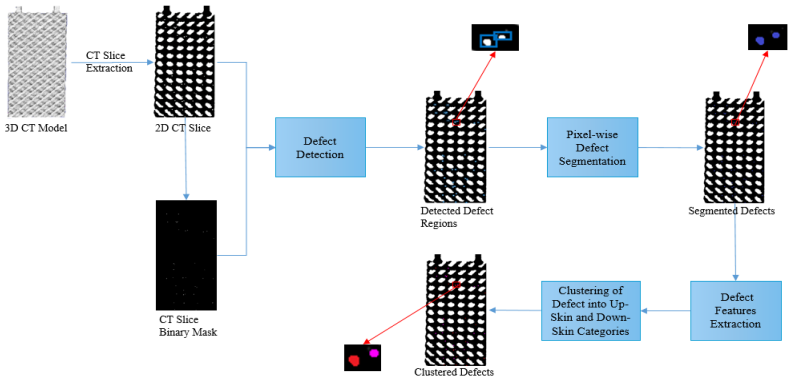

Figure 2. Overview of the proposed pipeline: a 3D CT volume is decomposed into X–Z slices with binary masks, surface defects are detected via a YOLO model and segmented by U-Net, and extracted features are clustered into up-skin and down-skin groups.

- Specimen manufacturing: Ti-6Al-4V lattice specimens were fabricated on a Renishaw AM 400 L-PBF system using plasma-atomized powder (d_{50}=34 µm). The process parameters adopted were 135 W laser power, 55 µm point distance, and 45 µs exposure time with meander scan strategy. Room temperature was used on the build plate in argon atmosphere ($O_2 \leq 500$ ppm). CT scan specifications revealed voxel size of 9.30 µm along all directions. Lattice structures were 6×6 mm in XY plane with a height of 14 mm, and the total part height was between 16-16.5 mm. Based on these measurements, 2 mm alignment tags were added to specimens to allow precise data alignment and future analysis.
- Micro-CT imaging: Samples were scanned with a high-resolution X-ray micro-CT (LE6 filter, 0.4× lens) using 80 kV Source voltage, 7 W source power, 1.5 s exposure time, 24012 projections, source–sample distance 23.02 mm, detector–sample distance 103 mm.

2.2. Proposed pipeline

In this work as shown in Figure 2, the original 3D CT volume is first decomposed into a series of X–Z 2D slices. Binary masks are generated offline to build training targets (defect centers and bounding boxes via 2D connected components); the detector itself is trained on raw CT slices. Once the YOLO network has learned to detect 2D surface defect regions on these slices, each detected surface defect is cropped and forwarded to a U-Net architecture for precise segmentation. Finally, morphological and intensity features are extracted from each segmented defect and clustered into two groups—up-skin and down-skin—shown in purple and red, respectively.

2.3. Defect detection and clustering

To distinguish 2D surface defects in a certain manner to identify down-skin and up-skin defects, X–Z CT slices were utilized. Slice-wise defects are attributed to the nearest labeled up- or down-skin surface region based on local orientation relative to the build direction; a one-voxel tie-break resolves boundary ambiguities. Then, a two-stage approach with the YOLO and U-Net models were utilized to perform defect detection.

- Image preprocessing: Binary masks are generated offline and lightly denoised to build training targets for YOLO.
- YOLO Training: Model trained on 80/20 split with batch size 16, 300 epochs, learning rate 0.01 to detect defect regions. At inference, the detector consumes raw CT slices only (no mask input).
- Pixel-wise segmentation with U-Net: Performs pixel-level segmentation within YOLO bounding boxes (200 epochs, learning rate 0.001, batch size 4).
- Defect feature extraction: Calculates defect characteristics including height (pixels), area, circularity, eccentricity, solidity, equivalent diameter, and perimeter.
- Defect clustering: Groups defects by structure using K-means (K = 2) algorithm and visualizes clusters with colored contours.

3. Results and discussion

We analyze the performance of the two-stage framework, where YOLO detects defect regions and U-Net refines them for precise pixel-level segmentation.

3.1. Defect detection performance using YOLO

The first stage uses YOLOv5 for defect detection, evaluated through loss convergence, precision–recall, and confusion matrix analyses.

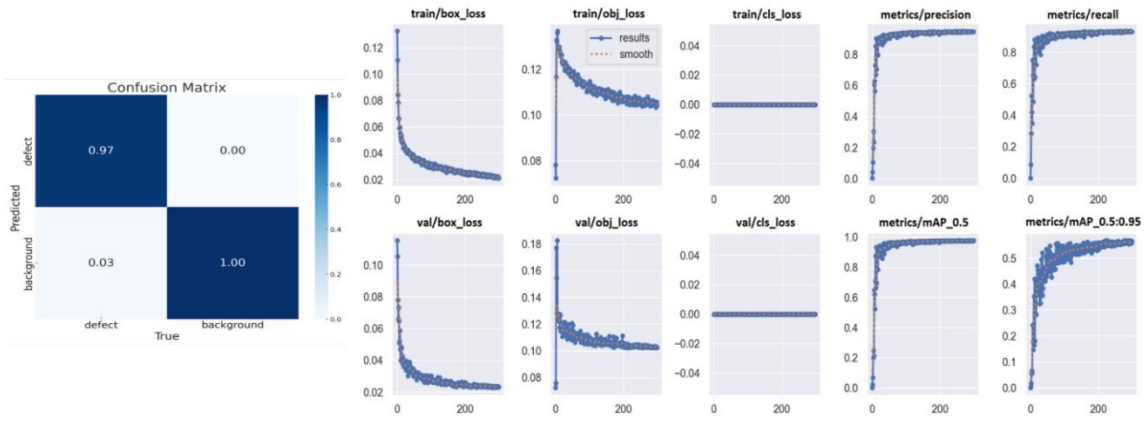

Figure 3. YOLOv5 model performance evaluation: Training/validation loss curves, metrics progression, and confusion matrix showing 97% defect detection accuracy with 100% background classification.

- Loss curves and convergence analysis: All the loss curves (box, object and classification) outlined in Figure 3, converge fast—reaching steady state around epoch 150 with near-zero classification loss—indicative of stable training without overfitting and good-quality, well-separable labels, while precision and recall improve rapidly above 0.9 and the model achieves mAP@0.5 ≈ 0.97 and mAP@0.5:0.95 ≈ 0.95, indicative of very good localization accuracy and generalization.
- Confusion matrix evaluation: According to the confusion matrix outlined in Figure 3, the model effectively detects 97% of 2D defects and identifies background 100% correctly. The false negative rate (3%) is low enough for segmentation-based tasks. The above results authenticate YOLO's applicability for coarse-level defect localization for X-ray CT images.

3.2. Pixel-wise refinement using U-Net

The U-Net model was employed to refine YOLO-generated bounding boxes through pixel-wise fine-grained segmentation. The Dice loss was chosen to tackle class imbalance and refine overlap accuracy between prediction and ground truth masks.

3.2.1. Loss convergence analysis

As can be seen from Figure 4a, both the training and validation Dice losses converge rapidly within the first 20 epochs and then flatten at a level of around 0.29, which suggests good learning and no overfitting. The two curves closely track each other, suggesting good generalization of the U-Net model to unseen data and effective representation of the morphology of defects at pixel-level accuracy.

3.3. Statistical analysis of defect clusters in up-skin and down-skin regions

The dataset comprises 600 CT slices with 64,974 surface-connected defect instances in total, of which 36,781 are attributed to up-skin (56.6%) and 28,193 to down-skin (43.4%). On average, we observe 108.3 defects per slice.

Clustering analysis reveals distinct morphological differences between up-skin and down-skin surface defects. As shown in Figure 4b, down-skin clusters exhibit significantly larger defect sizes (>2500 pixels per slice) and lower circularity values (0.55-0.6), indicating irregular, elongated morphologies. In contrast, up-skin clusters show smaller defect sizes (<1000 pixels) and higher circularity (0.75-0.8), reflecting more spherical shapes. These findings confirm that surface orientation dominantly affects defect formation, with unsupported down-skin geometries promoting large, irregular defects due to thermal instability, while up-skin regions maintain controlled, spherical defect development.

3.4. Discussion and comparative evaluation

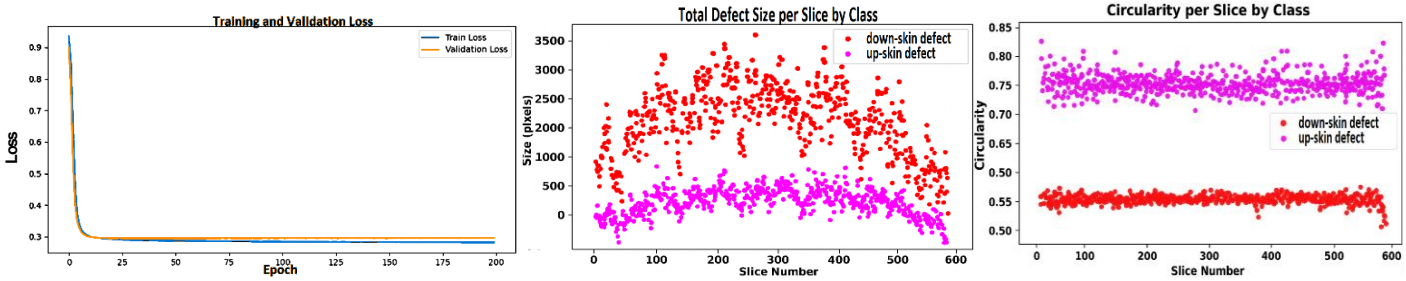

(a) **(b)**

Figure 4. (a) U-Net segmentation Dice loss over 200 epochs, showing both training (blue) and validation (orange) losses rapidly decreasing and stabilizing around 0.29. (b) Scatter plot of total defect area and circularity per CT slice by class, illustrating consistently larger and more irregular down-skin defects (red) compared to up-skin defects (purple) across 600 slices.

This work presents a new approach for applying 2D surface defect analysis on LPBF parts that eliminates the limitations of current approaches. Global thresholding, morphological filtering, and connected-component labeling were the conventional techniques that required enormous manual adjustment, were quality-dependent upon the CT scan, and lacked the ability to incorporate contextual information like defect placement in up-skin or down-skin regions with drastic influences on defect morphology. The proposed solution employs a three-stage pipeline involving YOLO for rapid defect candidate detection, U-Net for precise pixel-level segmentation, and geometric feature-based unsupervised clustering. This deep-learning pipeline learns directly from CT data and minimizes manual preprocessing (e.g., global thresholding). Binary masks are used only to build training labels; at test time the detector runs on raw CT (no mask). It scales to large slice stacks (real-time left for future work) and shows stable performance (Dice loss ≈ 0.29). The outcomes illustrate successful differentiation among defect types and show that down-skin region defects have higher areas and lower circularity measures, indicative of their elongated and irregular shapes, whereas up-skin defects are still small and practically circular, as expected from Figure 1. These differences are both locally and statistically significant, validating conceptual justification that the same geometries in STL models are translatable to visibly distinct shapes upon print based on orientation.

Modularity of the pipeline enables future extensions like reconstructing 3D pores by linking slice-level detections between slices (3D connected components) to obtain pore volumes and meshes. In parallel, we will evaluate 2D profile/areal surface roughness and relate it to the observed slice-level defect statistics. These representations can, in turn, be used as priors and training targets for generative models for morphology prediction in future layers and for aiding adaptive process control.

3.5. Conclusion

In this work, we have suggested a fully automated pipeline to extract crisp insights into up-skin and down-skin defect structures in 3D CT volumes. Using volume decomposition into slices in the X–Z planes, generation of corresponding binary masks, and training a YOLO detector optimized by U-Net segmentation, we can carry out accurate localization and boundary definition of defects. The derived morphological and intensity features then enable strong clustering into up-skin (purple) and down-skin (red) clusters, which recognize their disparate characteristics. This-separated perception of defect morphology unravels the potential for future generative AI–based approaches: with each step of a CT scan sequence, we can predict the evolution of defect structures in subsequent scans. This predictive capability will allow more intelligent choices at each stage of the 3D printing process—paving the way toward adaptive, potentially real-time adjustments in future work to accommodate anticipated defect formations and improving overall print quality.

4. References

[1] Chahal V, Taylor RM. A review of geometric sensitivities in laser metal 3D printing. Virtual Phys Prototyp. 2020;15(2):227–241.
[2] DebRoy T, Wei HL, Zuback JS, Mukherjee T, Elmer JW, Milewski JO, Beese AM, Wilson-Heid A, De A, Zhang W. Additive manufacturing of metallic components – Process, structure and properties. Prog Mater Sci. 2018; 92:112–224. doi: 10.1016/j.pmatsci.2017.10.001.
[3] McGregor M, Patel S, Zhang K, Yu A, Vlasea M, McLachlin S. The downside of downskin: an overhang ratio to digitally evaluate printability of complex architectures by laser powder bed fusion additive manufacturing. OSF Preprints. 2023; doi:10.31224/3074
[4] McGregor M, Patel S, McLachlin S, Vlasea M. Architectural bone parameters and the relationship to titanium lattice design for powder bed fusion additive manufacturing. Additive Manufacturing. 2021; 47:102273.
[5] Fuchs P, Kröger T, Garbe C. Defect detection in CT scans of cast aluminum parts: A machine vision perspective. Neurocomputing. 2021; 450:135–147.
[6] Acharya P, Chu TP, Ahmed KR, Kharel S. A deep learning approach for defect detection and segmentation in X-ray computed tomography slices of additively manufactured components. Int J Artif Intell Appl. 2022;13(4):1–8.
[7] Taherkhani K, Eischer C, Toyserkani E. An unsupervised machine learning algorithm for in-situ defect-detection in laser powder-bed fusion. J Manuf Process. 2022; 81:476–489.
[8] Kasperovich G, Becker R, Artzt K, Barriobero-Vila P, Requena G, Haubrich J. The effect of build direction and geometric optimization in laser powder bed fusion of Inconel 718 structures with internal channels. Materials & Design. 2021; 207:109858
[9] Shange M, Yadroitsava I, du Plessis A, Yadroitsev I. Roughness and near-surface porosity of unsupported overhangs produced by high-speed laser powder bed fusion. 3D Printing and Additive Manufacturing. 2022;9(4):288-300.